Combustion and Flame 197 (2018) 182–196

Contents lists available at ScienceDirect

Combustion and Flame

journal homepage: www.elsevier.com/locate/combustflame

The evolution of autoignition kernels in turbulent flames of dimethyl ether

Andrew R.W. Macfarlane*, Matthew Dunn, Mrinal Juddoo, Assaad Masri

School of Aerospace, Mechanical and Mechatronic Engineering, The University of Sydney, J07 - Mechanical Engineering Building, NSW 2006, Australia

ARTICLE INFO

Article history:
Received 6 March 2018
Revised 25 July 2018
Accepted 25 July 2018
Available online 22 August 2018

Keywords:
Turbulent flames
Autoignition
High-speed imaging
Lifted flames
Dimethyl ether
Heat release imaging

ABSTRACT

Simultaneous planar laser-induced fluorescence (PLIF) imaging of CH_2O and OH was performed at a repetition rate of 10.kHz, jointly with chemiluminescence to explore autoigniting dimethyl ether (DME) flames in a hot vitiated coflow burner. The focus of the study is the imaging of the flame stabilization region and the temporal evolution of ignition kernels upstream of the flame base. Results detail the evolution of kernels throughout their formation, growth and final merging with the flame base. The ignition events were explored for a range of different fuel premixing and dilution ratios over two coflow temperatures which result in different lift-off heights. Images of CH_2O and OH over the entire flame length show that not only is the lift-off height much higher at low coflow temperatures, but that the fluctuations are more intense and the region of kernel formation is larger both radially and axially. In these autoignition stabilized flames, increased premixing leads to the lift-off height and location of the maximum kernel formation rate being further downstream. Transient 1-D simulations of hot coflow products opposed against jet fuel mixtures identify that the overlap of CH_2O and OH PLIF signals are a reliable marker of heat release in autoignition kernels. Measurements indicate that for the high coflow temperature cases, on average, the heat release of individual kernels is low, despite the high total kernel formation rate. This can be correlated to the slow growth rate and elongated aspect ratio of the kernels. For low coflow temperature cases, kernels are growing faster and have high heat release rates with near unity aspect ratios.

1. Introduction

Dimethyl ether (DME) is a promising alternative to conventional fossil fuel-derived diesel in compression ignition engines [1]. Another application of DME is in land-based gas turbines where it can potentially replace compressed natural gas (CNG) and liquefied petroleum gas (LPG) as a cleaner fuel [2]. DME has several desirable combustion properties such as a high cetane number, low autoignition temperature and a low sooting propensity by virtue of the fuel bound oxygen. However, due to the multiple competing chemical pathways leading to autoignition [3], the low-temperature chemistry of DME is significantly more complicated compared to simpler fuels such as methane and syngas.

The autoignition combustion process compared to freely propagating flames contains significant differences in terms of low-temperature chemistry and chemical time scales; and as such has received considerable attention both numerically and experimentally for a variety of fuels. Experimental studies have mostly focused on three jet in hot coflow burner (JHC) configurations, which provide conditions that are comparable to practical applications such as: exhaust gas recirculation (EGR) in gas turbines. These three burner configurations are: (i) The jet in a hot vitiated coflow (VCB) investigated by Cabra et al. [4,5], Gordon et al. [6,7], Oldenhorf et al. [8–11] and Arndt et al. [12,13], (ii) fuel jet in heated air, Markides and Mastorakos [14] and, (iii) Mild combustion by Medwell and Dally [15-17]. The JHC is studied extensively using hydrogen [5,7,18,19], methane [9,20] and more recently heptane [21], which have shown qualitatively similar stability with the lift-off height being strongly dependent on the temperature of the coflow. High-speed imaging of chemiluminescence as well as laser-induced fluorescence (LIF), have also shown that autoignition is initiated by the formation of kernels upstream of the flame base [6]. Oldenhof et al. [8,9] have used ignition statistics to identify autoignition as the main stabilizer, indicating ignition kernels form upstream then grow and convect downstream to meet the flame base. Ardnt et al. [22,23] have used pulsed methane jets in a hot vitiated coflow to confirm that ignition occurs in very lean mixtures where the scalar dissipation rates are low.

* Corresponding author.
E-mail addresses: amac7548@uni.sydney.edu.au (A.R.W. Macfarlane), matthew.dunn@sydney.edu.au (M. Dunn), mrinal.juddoo@sydney.edu.au (M. Juddoo), assaad.masri@sydney.edu.au (A. Masri).

https://doi.org/10.1016/j.combustflame.2018.07.022
0010-2180/

Using heated air to initiate autoignition, Markides and Mastorakos studied the effect of turbulence on ignition delay times. They have shown that increasing the turbulent length scale by altering the fuel nozzle diameter increases the ignition delay time [32]. However, increased Reynolds number for the same jet diameter increases entrainment of hot coflow fluid and hence lowers the location where initial reactions occur [33]. In the third configuration of Mild combustion, autoignition remains the dominant mode of stabilization. However, Medwell et al. [16] highlight an 'apparent' lift-off height upstream of a faintly attached OH tail to the exit nozzle. This is in contrast to the more distinct OH gradient at the flame base in the case of the JHC burner.

Numerical studies on the autoignition of turbulent flames may be classified in two broad categories: direct numerical simulation (DNS) and either large eddy simulations (LES) or RANS with a relevant combustion model. DNS studies have established that autoignition events occur mostly in regions of lean mixture fractions (most reactive mixture fractions) and at low scalar dissipation rates [24,25]. Echekki and Chen [26] have shown kernels to initiate in lean mixtures but the flame propagation crosses stoichiometric contours leading to burning of richer mixtures. Sreedhara and Lakshmisha [27] have shown vortex shedding in 3-D DNS produces faster ignition delay times than 2-D DNS. Cao and Echekki [28] performed 3-D DNS, indicating lean autoignition kernels initially propagate in a similar most reactive mixture fraction field then extending into rich regions; a conclusion also supported by Echekki and Chen [26]. Further details on autoignition propagation and the coflow burner topic may be found in the review by Mastorakos [29]. DNS studies by Yoo et al. [3,30] used chemical explosive modes to demonstrate that lifted hot coflow flames are stabilized by autoignition. The oscillation and upstream 'jumps' in the flame base are due to kernel merging events, where premixed stabilization is not responsible for any upstream propagation.

Large Eddy (LES) and Reynolds Average Navier Stokes (RANS) simulations of autoigniting flames have been performed for the various burner configurations mentioned earlier. Using RANS with a composition probability density function (PDF) and detailed chemical kinetics Gordon et al. [31,32] analysed the concentration of radicals and transport budgets in JHC flames at different coflow temperatures. Numerical simulations have identified that a radical build-up (HO_2, H_2O_2 and CH_2O) occurs in the lead-up to autoignition [33]. There is a transition from a convective-reactive balance when autoignition prevails to a diffusive-reactive balance when premixed flame propagation is the dominant mode of stabilization [34]. Laminar DME autoigniting flames [35] have shown a transition from autoignition to flame propagation stabilization for increased coflow temperatures. Further PDF methods by Masri et al. [36] showed the ignition and hence stabilization to be largely controlled by chemistry rather than mixing rates. LES simulations [20,37,38] of autoigniting methane flames have confirmed the concept of the most reactive mixtures being responsible for initiating autoignition.

Existing knowledge on autoignition acquired from earlier studies should carry across to DME, notwithstanding the additional complexities of chemical kinetics. The formaldehyde radical (CH_2O) has been used as a low-temperature and ignition marker in high-pressure experiments [39] to identify the first and second stages of ignition for DME [40]. Imaging of OH and CH_2O LIF was performed simultaneously [17,41–44] to identify low and high-temperature regions, where their spatial overlap is employed as a marker for heat release [45] as is done in this work.

Reliable chemical kinetic mechanisms are needed to compute the autoignition delay times which are subsequently used to predict lift-off heights in laminar [46,47] and turbulent [48] autoignition flames. Since DME displays mild negative temperature coefficient (NTC) behaviour and has significant low-temperature reactions [49] there are potential difficulties in obtaining reliable mechanisms to correctly predict ignition delay times. Three mechanisms for DME are commonly applied (NUIG Mech_56.54 [50], NUIG Aramco Mech 1.3 [51], and Zhao et al. [52]) with the former showing the best agreement with measured data [53,54]. Reduced mechanisms such as Pan et al. [55] remove certain minor pathways to minimize computational cost compared to the large parent NUIG Mech_56.54 [50] mechanism. The reduced mechanism has been shown [55] to represent experimental delay times for DME at a range of ignition temperatures, where species, OH and CH_2O are also well represented.

The simplest reactor is typically the 0-D homogenous constant pressure reactor, which can identify delay times and additionally demonstrate negative temperature coefficient behaviour described by Li et al. [56]. This was also confirmed by Echekki and Ahmed [57] who demonstrated DME's dual stage ignition. Owing to imposed scalar dissipation from turbulent flow fields, opposed flow simulations between cold fuel and heated oxidants are often used. The opposed flow reactors show S-shaped plots of temperature versus strain rate [58]; with autoignition found to occur only for strain rates below a critical value. Increased DME fuel fraction with N_2 and increased strain rates have the effect of increasing the ignition temperature ranging between 900–1300 K [59]. Transient counterflow flames (used in this study) with a heated oxidant against a fuel jet [13, 40] have been used to identify how increased strain rate or scalar dissipation rate serve to increase delay times.

The current paper builds upon previous work [60] that studied autoignition and flame stabilization processes in DME flames primarily using chemiluminescence as a diagnostic tool. It addresses the influence of ignition kernels and their dependence on the flame base stabilization. A link between the formation rates and relative heat release of autoignition events for varying coflow temperatures and premixing/dilution ratios with DME is observed. Joint PLIF of OH and CH_2O is performed to resolve the flame structure in the stabilization zone and kernel heat release measurements are reported for a range of coflow temperatures.

2. Experimental setup

2.1. Hot coflow burner

The hot coflow burner in this experiment is similar to that studied by Cabra et al. [4,5] and used previously at the University of Sydney [20,60]. The diameter of the coflow is 197 mm with $\sim$1800 $\times$ 1.6 mm diameter holes to stabilize the lean H_2/air flames; the coflow shrouds the central fuel jet, having an inside diameter (D_J) of 4.45 mm. The burner produces a simplified axisymmetric geometry making modelling and optical access very accessible. By varying the shrouded H_2/air equivalence ratio, the required coflow temperature is established such that for this experiment a constant bulk burnt velocity of $U_C = 4$ m/s was maintained. The hot coflow provides a cone of combustion products that remains uncorrupted by laboratory air for about 60 D downstream of the stabilising plate. This region is referred to as the 'valid cone' within which all subsequent measurements are restricted.

Conditions selected for further study are listed in Table 1 along with relevant flame properties. In addition to pure DME, three other mixtures are investigated to study the effects of partial premixing with air and dilution with nitrogen. Table 1 lists two mixtures of DME with air for two volumetric ratios: 1:1 and 3:1 (three parts air and one part DME) and one dilution ratio of DME and N_2 at 3:1 (three parts N_2 and one part DME). Mean lift-off heights and their RMS values for a range of coflow temperatures at the premixing ratios studied here can be found in a previous publication [60]. Each fuel is investigated at two coflow temperatures: a lower temperature (around $T_c = 1250$ K) and a higher temperature coflow of

Table 1
Fuel jet compositions studied: premixing ratio, diluent gas and jet velocity.

Jet mixing	Pure DME		air:DME = 1:1		air:DME = 3:1		N_2:DME = 3:1		air:DME = 3:1	
U_J (m/s)	50		50		50		50		100	
Re_J	38,610		22,990		16,650		16,683		33,293	
T_c (K)	1225	1400	1250	1400	1275	1400	1275	1400	1275	1400
ξ_{st}	0.06	0.06	0.11	0.11	0.21	0.20	0.17	0.16	0.21	0.20

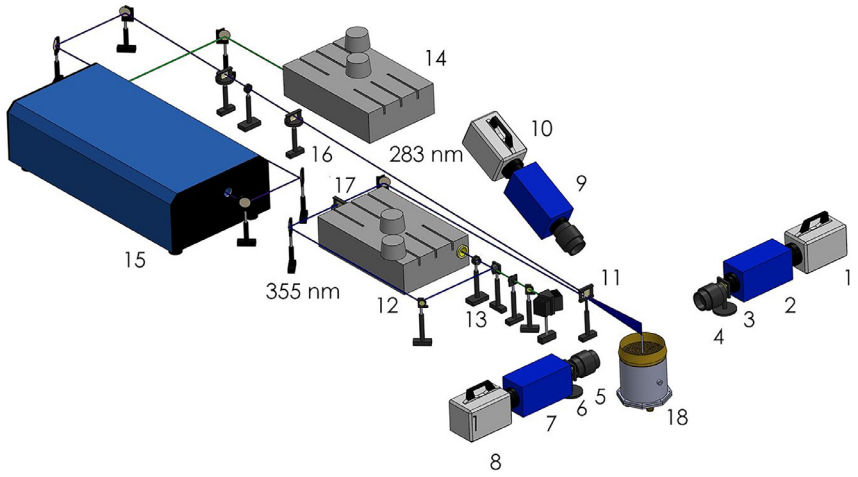

Fig. 1. 10 kHz experimental setup: (1) OH PLIF camera (2) OH Intensifier (3) Semrock FF01-315/15-50 (4) OH UV collection lens (5) 85 mm $f_{\#} = 1.2$ lens (6) Semrock FF02-409/LP-25 (7) CH_2O Intensifier (8) CH_2O PLIF camera (9) CH^* IRO (10) CH^* camera (11) Cylindrical lens (12) CH_2O Edge wave laser (13) Dichroic mirror (14) OH Edge wave laser (15) OH Dye laser (16) Keplerian telescope (17) Galilean telescope (18) Coflow burner.

$T_c = 1400$ K. The low coflow temperature corresponds to a high average lift-off height of $x/D \approx 35$, resulting in coflow temperatures ranging from $T_c = 1225$ K to $T_c = 1275$ K for the fuel mixtures outlined in Table 1. A constant high coflow temperature of $T_c = 1400$ K was used for all premixed and diluted cases; producing a similar, lower lift-off heights of $x/D \approx 7$. The jet velocity of $U_J = 50$ m/s is selected such that the flame base remains, for all cases, within the valid cone while the jet Reynolds number (Re_J) is sufficiently high. The partially premixed case of air:DME = 3:1 is also studied at a higher jet velocity of $U_J = 100$ m/s to report the effects of higher mixing rates. Table 1 also shows the stoichiometric mixture fraction (ξ_{st}), which increases slightly with decreasing coflow temperature due to a slight change in the composition of the hot coflow. That is, a $T_c = 1225$ K coflow ($\varphi = 0.31$) has 14% O_2 content while a $T_c = 1400$ K coflow ($\varphi = 0.39$) has 12% O_2 content from the products of a Cantera [61] equilibrium solver with H_2/air.

2.2. High-speed imaging setup

An experimental setup employing simultaneous high–speed (10 kHz) planar laser-induced fluorescence (PLIF) of OH and CH_2O combined with out of plane chemiluminescence imaging is applied in this study. This setup enables the investigation of spatio-temporal dynamics from OH, CH_2O and visible broadband chemiluminescence fields with respect to kernel ignition and growth. The PLIF experimental setup diagram illustrating the orientation of the three cameras employed relative to the laser beams and flame is presented in Fig 1.

The OH radical was fluoresced using an Edgewave Nd-YAG laser (Edgewave IS8II -E) that pumps a tunable dye laser (Sirah Credo). This system produced a wavelength of 283 nm that overlapped onto the strong $Q_1(6)$ transition for $A^2\Sigma^+ \leftarrow X^2\Pi(1,0)$ excitation, where the energy was measured at 0.14 mJ/pulse. The OH PLIF signal was collected with a 150 mm focal length, $f_{\#} = 1.65$, 6 element UV lens (2 of CVI LAPQ-300.0-60.0-PM + APMQ-300.0-60.0-PM) resulting in a mapped pixel resolution of 56 µm/pixel. Interferences were blocked using a 15 nm FWHM band pass filter centred at 315 nm (Semrock FF01-315/15-50) and a coloured glass filter (1 mm, UG-11) combined with a short intensifier gate time of 200 ns.

Excitation of the CH_2O PLIF was achieved using the third harmonic at 355 nm from an Nd:YAG (Edgewave HD30II-E) laser. Excitation at 355 nm probes the weaker rotational transitions within the $\tilde{A}^1A_2 - \tilde{X}^1A_1 4_0^1$ vibronic state. The 355 nm beam was measured to be 25 mm high and 350 µm wide at the probe volume with an energy of 3.3 mJ/pulse. The CH_2O PLIF signal was collected with an 85 mm, $f_{\#} = 1.2$ lens resulting in a mapped pixel resolution of 56 µm/pixel. A combination of a 409 nm longpass filter (Semrock FF02-409/LP-25) the 355 nm beam being p-polarized and a short intensifier gate time of 200 ns removed interferences.

Collection of the OH and CH_2O signals were obtained perpendicular to the laser sheet using two high-speed CMOS cameras after imaging with two staged (LaVision HS-IRO) intensifiers. The mapping between the CH_2O and OH cameras was achieved using a metal plate with uniformly spaced 1 mm holes; after which a polynomial warping and correction was applied. The image mapping between the OH and CH_2O PLIF cameras were achieved with a mean pixel mapping error of 0.4 pixels and a maximum error of 0.8 pixels which is acceptable for [CH_2O] x [OH] product imaging.

Cross-talk interferences between the CH_2O and OH PLIF signals were eliminated by delaying the 355 nm beam from the 283 nm beam by 200 ns. Beam energy fluctuations for both the 355 and 283 nm were acquired using photodiodes (Thorlabs DET10A) and recorded using a digital storage oscilloscope (Tektronix DSA70404C). Beam expansion telescopes were utilized to match the focal point of the 283 and 355 nm beams at the probe volume as well as to expand the beams in the vertical direction. The spatially overlapping region for both OH and CH_2O PLIF signals was 20 mm (height) x 43 mm (width). The signal to noise ratio, (SNR: the ratio of a mean signal to the RMS) for OH and CH_2O PLIF is around 11 if the mean signal is around 300 counts for both. However, the peak count levels for this setup of OH and

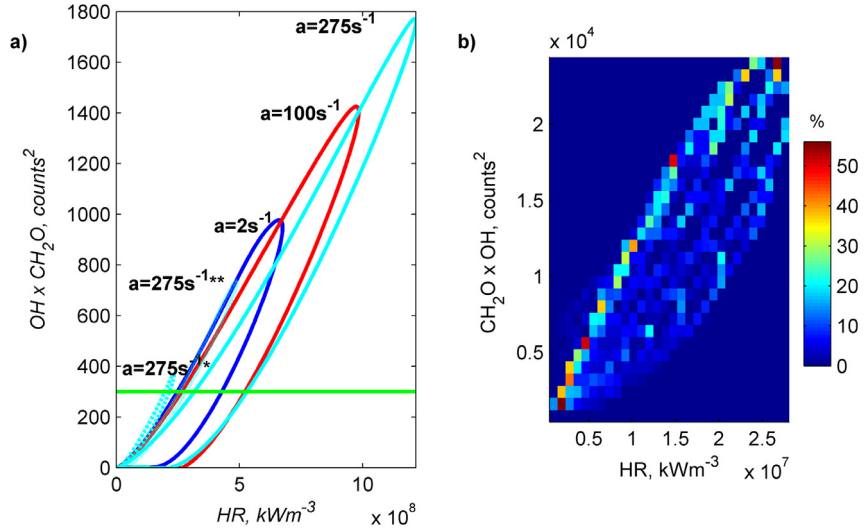

Fig. 2. Results for heat release (HR) and the product, CH_2O x OH, computed for a pure DME jet opposing hot coflow products from a premixed H_2/air flame at 1400 K ($\varphi = 0.39$). (a) Profiles of the product CH_2O x OH vs. HR plotted for strain rates of $a = 2\,s^{-1}$, $50\,s^{-1}$ and $250\,s^{-1}$ at 300 µs post autoignition (solid lines). For the case of $a = 250\,s^{-1}$, two additional profiles are also shown for times before (*) and during (**) ignition. The horizontal line shows a sample value of the product CH_2O x OH for which a histogram for the computed values is determined (b) Color contours of the probability density of the correlation between the product CH_2O x OH and HR is obtained from the entire set of 20 simulations.

Table 2
Maximum CH_2O signal yield from a Bunsen flame for varying equivalence ratios using DME and CH_4 fuels.

DME Equivalence ratio (φ)	CH_2O signal
1	240
2	512
5	912
CH_4	
3	27

CH_2O are ~1100 and ~320, respectively and at these signal levels, the SNR's are 20 and 11, respectively. The third camera collecting the chemiluminescence was oriented at 20° to the other two PLIF cameras. The signal was collected with a visible 50 mm, $f_{\#} = 1.2$ Nikon lens and this has included broadband chemiluminescence. A separate spectroscopic analysis confirmed that chemiluminescence from these DME non-sooting flames is mostly due to CH*. The image size was 77 mm x 77 mm and had a mapped pixel resolution of 100 µm/pixel.

The excitation of CH_2O with relatively low laser energies from the third harmonic of a high-repetition laser at 355 nm is applicable for DME (but not CH_4) flames due to the amount of CH_2O produced. The increased CH_2O signal above the background collected by this system for a DME Bunsen flame using different equivalence ratios compared to CH_4 is presented in Table 2. The yields are based off an unquantified comparison; excluding population density and quenching for a 355 nm laser for the corresponding fuels. For comparison, 1-D premixed flames for CH_4 and DME at stoichiometric values gave a mole fraction of 9.5×10^{-4} and 8×10^{-3} respectively. The close to an order of magnitude difference in mole fractions is consistent with the difference in fluorescence signals obtained for these two fuels.

3. Correlation of OH x CH_2O with heat release

Results from multiple transient opposed flow simulations are presented in Fig. 2. The flow configuration corresponds to opposed streams of pure DME on one side against combustion products from a premixed H_2/air flame at an equivalence ratio of $\varphi = 0.4$ and $T = 1400$ K. The Cantera code [61] with a transient Ember solver [62] is employed using multicomponent diffusion and the reduced Pan mechanism for DME which consists of 29 species and 66 reactions [55]. Twenty simulations are repeated for strain rates spanning the range $a = 2$–$500\,s^{-1}$ and the results of heat release (HR in kW/m^3) versus the "expected LIF counts" from the product of OHxCH_2O are plotted. Samples of these results are shown in Fig. 2a for strain rates of $a = 2\,s^{-1}$, $50\,s^{-1}$ and $250\,s^{-1}$ at 300 µs post autoignition. For the case of $a = 250\,s^{-1}$ two additional profiles are also shown for times before (*) and during ignition (**).

The "expected LIF count" from the product of CH_2O x OH is representative of the LIF signal that would have been obtained from the calculated concentrations. To determine this, the computed OH and CH_2O concentrations are corrected for quenching and Boltzmann population distribution as follows: The OH LIF correction is well understood and has been performed in accordance with Kamura et al. [62]. However, the quenching properties of the polyatomic molecule, CH_2O, is not as well understood and multiple groups have approximated the quenching characteristics using a temperature based correlation $Q \propto T^{-0.5}$ [45,63–65]. In this paper, an approximate species-based correction is applied by obtaining temperature based quenching cross sections of N_2 and O_2 from Yamasaki and Tezaki [66]. They showed that both the more passive quencher, N_2, and aggressive quencher, O_2, (which is approximately 8 times greater than N_2) have very similar negative linear gradients for an Arrhenius fit with temperature. This linearity for the two extreme quenchers justified the assumption that the other known room temperature (~300 K) quenchers (DME, CO_2, CO, NO and CH_2O) behave in a similar way, with the room temperature quenching cross sections [66,67] used for the intercept on the Arrhenius fit. Finally, the Boltzmann correction for a 355 nm excitation of CH_2O was used from the work of Kyritsis et al. [68] and Clouthier and Ramsay [69].

Bins of fixed values of product CH_2O x OH (as illustrated by the horizontal line of Fig. 2a) are then employed to construct a histogram of HR from the intersection of the 20 simulations. This process is repeated to extract the correlation between HR and the "expected LIF counts" for the product of CH_2O x OH as shown in Fig. 2b. The color bar shown on the right-hand side of Fig. 2b

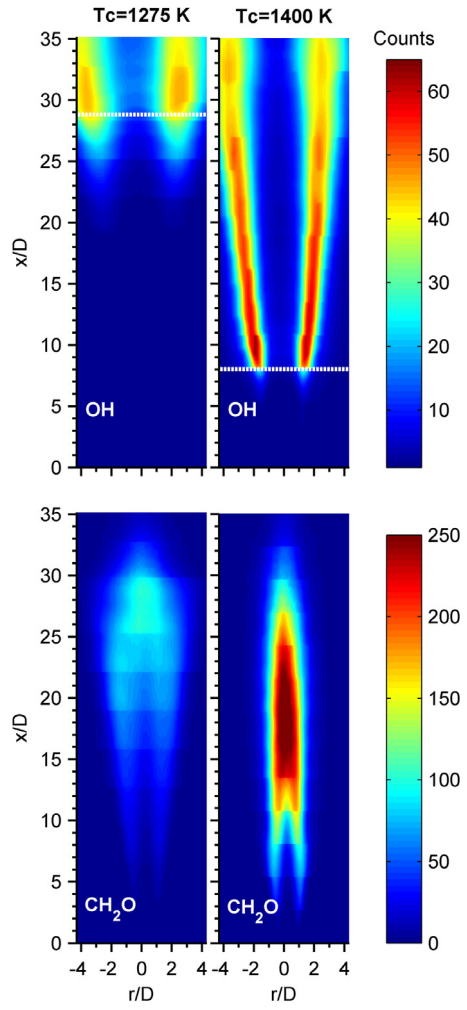

Fig. 3. Average stacked OH and CH_2O PLIF results for partial premixing, air:DME = 3:1 $U_J = 50$ m/s with coflow temperatures of $T_c = 1275$ K (left column) and $T_c = 1400$ K (right column). Colour bars describe the signal counts and correspond to each OH and CH_2O row respectively. The horizontal line indicates the mean OH lift-off height.

marks a probability density for the joint correlation between HR and the product CH_2O x OH. The data has been presented by normalizing each row to form a color map that produces the most probable heat release values for a given CH_2O x OH product. That is for a given product CH_2O x OH of ~6000 counts^2, there is 50% confidence that this produces 5×10^6 kW/m^3 of heat, while 20,000 counts^2 has a more uniform probability of ~20% for an interval: 1.8–2.5 $\times 10^7$ kW/m^3. The lean branch (upper bound) from the simulation has a better correlation of CH_2O x OH to heat release. Furthermore, solutions from the transient solver were collected at ~10 μs intervals post autoignition. Autoignition is defined when the OH signal exceeds ~100 counts (after LIF correction) as per the experiment. While the correlation between heat release and the product of CH_2O x OH seems to break down for steady diffusion or partially premixed flames [64,65], it remains valid for the transient state where auto-ignition is occurring as relevant to the flows considered here.

4. Experimental results

Selected mean and instantaneous LIF-OH and LIF-CH_2O structures (such as those shown in the images of Fig. 3) are reported here with a particular focus on the upstream region close to the stabilization point. Section 4.1 presents flame mean images for the premixing of air:DME = 3:1, $U_J = 50$ m/s, $T_c = 1400$ K and $T_c = 1275$ K. Section 4.2 shows cases of instantaneous images for a pure DME jet obtained from both PLIF and chemiluminescence results."

Sections 4.3–4.9 analyse kernel dynamics: formation rates, growth rates, aspect ratios and kernel heat release. Formation rates and a 2-D map have been presented based on kernel formation centroids, while growth rates and kernel aspect ratios describe the physical kernel evolution. Finally, heat release results are obtained from the overlap between CH_2O and OH. Results for the relative differences in heat release from: high and low coflow temperatures, varying premixing/ dilution ratios are presented.

4.1. Mean flame signal: 3:1 = DME:Air $U_J = 50$ m/s

There are notable differences in both the OH and CH_2O fields and their spatial correlation between the high and low coflow temperature cases. It is observed in Fig. 3 that the OH initiation occurs at $x/D \approx 8$ and $x/D \approx 25$ for the $T_c = 1400$ K and $T_c = 1275$ K cases respectively; agreeing closely with the chemiluminescence lift-off heights presented in a previous publication [60]. The lift-off height is defined by the axial position for which OH has a peak gradient (d[OH]/dx) along a vertical line that intersects with the peak OH signal.

The radial OH width for the lower coflow temperature case ($T_c = 1275$ K) is much broader for all x/Ds despite the stoichiometric mixture fraction (ξ_{st}) being very similar. The low-temperature coflow case for $T_c = 1275$ K, has a peak in OH signal near the flame base, whilst at higher temperatures ($T_c = 1400$ K) the signal remains high for almost the full length of the flame with a peak signal closer to the jet centre. For the lower coflow temperature with $T_c = 1275$ K, the flame base (marked by the horizontal dashed line in Fig. 3) is not only much further downstream than that of $T_c = 1400$ K but appears to have a spatially wider OH profile. This is because at this downstream location of x/D~28, and for the same mixture fraction band, OH covers a broader spatial range because of the shallower gradients. It is evident that as the flame stabilization region transitions to a downstream axial location, it experiences different flow and mixing fields. However, the key factor remains that these transitions are induced by the co-flow temperature which changes the ignition delay times significantly but also influences the most ignitable mixture and the tolerable scalar dissipation rates. These trends are also consistent with transient laminar flame calculations for auto-igniting mixtures.

The initial formation of the CH_2O signal seen in Fig. 3 occurs in similar axial locations of $x/D \approx 6$ for both the high and low coflow temperatures and this is much earlier than the region of OH initiation. The location of the CH_2O radical relative to OH indicates that CH_2O is forming in richer regions where entrainment of the coflow is relatively small, also indicating lower temperatures.

The centreline containing unreacted fuel is indicated by the absence of LIF-CH_2O. The region of unreacted fuel is shorter for $T_c = 1400$ K extending to $x/D \approx 12$, whereas no CH_2O signal occurs until $x/D \approx 17$ for the low coflow temperature, $T_c = 1275$ K. The axial distance over which the entire CH_2O signal may be detected is somewhat similar between the coflow cases, extending to $x/D \approx 30$, which can be attributed to the comparable jet momentum of both flames. The radial narrowing of the CH_2O signal for the higher coflow temperature, $T_c = 1400$ K, leads to the hypothesis that the flame is burning in a different regime and a visibly more stable flame brush is observed in the region displayed.

The relative spatial formation of the OH and CH_2O species for the high and low coflow temperature is of interest as a marker of heat release and further reactivity. At higher coflow temperatures, $T_c = 1400$ K, CH_2O forms in the centre of the OH

branches for the axial locations where it is detected. In these regions the spatial overlap in the radial direction is minimal. A build-up of CH_2O for the lower coflow temperature ($T_c = 1275$ K) occurs directly below the flame base highlighting its importance before the formation of OH, where an axial and radial spatial overlap is observed compared to $T_c = 1400$ K. The accumulation of CH_2O radicals upstream of the flame base and OH is indicative of it being a low-temperature species, therefore, highlighting CH_2O's importance to the lead up to autoignition and hence stabilization to the flame. There is seemingly less dependence on the build-up of CH_2O below the OH flame base for $T_c = 1400$K, indicating a potentially different stabilization mechanism.

The relative build-up of OH and CH_2O at $T_c = 1400$ K is similar to that reported by Nomad et al. [70] for autoigniting laminar methane flames. However, the lower coflow temperature, $T_c = 1275$ K, is better represented by the MILD combustion autoigniting flames at a correspondingly lower relative temperature. The species accumulating in the pool of radicals leading to autoignition has been further verified in another laminar flame simulation by Deng et al. [35] with DME and Air.

4.2. Instantaneous kernel structure

A kernel refers to an island of LIF-OH (OH-kernel) or an island of chemiluminescence (CL-kernel) upstream of the respective OH or chemiluminescent flame base, overlapping LIF-OH and LIF-CH_2O is termed a HR-kernel (heat release kernel). The OH-kernels were extracted after the images were processed using a median filter. Other processing methods such as gradient sharpening techniques were also applied with negligible difference in the processing results. Therefore, it was determined that the noise processing method was not too sensitive for the issues of relevance here, namely: kernel growth rate, kernel aspect ratios or the heat release analysis. A pixel threshold was also applied, where it is noted an OH-kernel ignition event forms approximately three times above the background with the OH-kernel peak signal being more than an order of magnitude greater. As such the pixel thresholding was also not too sensitive in the processing analysis. The CH_2O signal of interest is that projected onto the OH-kernel and as such only required a background, beam and absorption correction was required.

Instantaneous samples from the time evolution of PLIF OH and CH_2O images collected from a pure DME jet with coflow temperatures: $T_c = 1225$ K and $T_c = 1400$ K is seen in Figs. 4 and 5, respectively; they present kernel formation and growth for 100 µs intervals. This sequence highlights the formation of a kernel, its growth and the varying perspective that the chemiluminescence camera observes. Kernels produced from a pure fuel jet compared to the increased premixed cases have been found to grow at a slower rate, which is further explored in Section 4.5 of the paper.

4.2.1. Pure DME Jet: $T_c = 1225$ K

The evolution of an autoignition event, OH-kernel, is defined by the number of OH pixels below the flame base exceeding a signal threshold above the background. The CH_2O kernel signal is the projected signal that overlaps onto the given OH-kernel. With this definition, the OH-kernel is forming in the first and second image of Fig. 4 and continues to grow in the following images.

The 2-D projected OH-kernel growth is somewhat spherical whilst advecting downstream with no upstream kernel centroid propagation. The OH-kernel is predominantly on the outside of the CH_2O sheet, two diameters from the jet centreline as observed in Fig. 4a and b. Having captured the signals simultaneously with sub-pixel spatial alignment between the OH and CH_2O cameras the product of the two signals given in Fig. 4c marks the overlap; where it is indicative of the heat release for the kernel. Heat release occurs from the first image, in row c of Fig. 4, and this is defined as kernel initiation. It is interesting to note that initially, the heat release distribution within the kernel is uniform until about 300 µs. Beyond this time, the distribution changes and the intensity becomes progressively stronger on the kernel's edge closest to the CH_2O sheet toward the centre of the jet. The pattern and trends in heat release are discussed in more detail later in the paper.

The chemiluminescence images shown in Fig. 4d capture a larger field of view than the PLIF images. Therefore, the lines B-B and A-A are the boundaries for the PLIF camera, while line C–C marks the location of the laser sheet. While the OH kernel initiates in the first image (row a) and the product CH_2O x OH indicates uniform heat release from it (row c), the chemiluminescence camera does not show any signal until 900 µs later (last frame of row d). It was noted earlier that the chemiluminescence observed here is largely due to CH^* and its delayed appearance is most probably due to a lower sensitivity in the camera although a mismatch between the production of CH^* and the product CH_2O x OH may also be a contributor. This latter aspect cannot be confirmed here and may be the subject of further investigations. Other cases have been found where a kernel forms in the chemiluminescence camera and not until it grows and crosses the laser sheet C–C does it appear on the PLIF camera. However, there are multiple occasions where an OH-kernel is observed in the PLIF OH image but not on the chemiluminescence camera.

4.2.2. Pure DME Jet: $T_c = 1400$ K

Increasing the coflow temperature from $T_c = 1225$ to $T_c = 1400$ K for the same pure DME jet changes many characteristics of the flame as shown in the sample sequence of images presented in Fig. 5. Kernels are forming much closer to the flame base, where the flame base is observed in the chemiluminescence images (row d) and appears in the LIF-OH frame as it cuts the line B-B. A similarly sized kernel to the low coflow temperature, $T_c = 1225$ K, forms in the first to the second image but the formation is much further upstream and closer to the flame base. Since the kernel forms so close to the flame base, it is consumed within 300 µs.

The OH-kernel forms further outside the CH_2O sheet relative to the lower $T_c = 1225$ K coflow case, where OH forms closer to the shear layer between the coflow and jet. The centre of the CH_2O sheet has a region of no signal owing to the fuel jet having no low-temperature reactions taking place at this upstream axial location. Furthermore, since the ignition kernel is further outside of the CH_2O layer, the overlap is identified to be smaller and this is explored in more detail later in the paper.

4.3. Formation of OH-kernels

This section tracks the formation and evolution of OH-kernels as markers of autoignition events. It is acknowledged here that initiation of kernels would have occurred upstream in fluid parcels populated by other species, such as CH_2O, before OH is produced however they cannot be conditioned appropriately for accurate diagnostics or are not measured (such as HO_2). For convenience, the centroids of OH-kernels are tracked in consecutive images, and the OH-kernel centroids are binarized, creating a 2-D formation map as seen in Fig. 6. The color bars indicate the rate of OH-kernel formation (kern/mm^2*s) at the relevant location. Heat release kernels (HR-kernels) as marked by the product of CH_2O x OH are discussed in a subsequent section of this paper.

From the formation map in Fig. 6a higher coflow temperature of $T_c = 1400$ K produces ignition OH-kernels at higher localized frequencies, where they form much closer to the exit nozzle and shear layer of the fuel jet. A decrease in coflow temperature, from

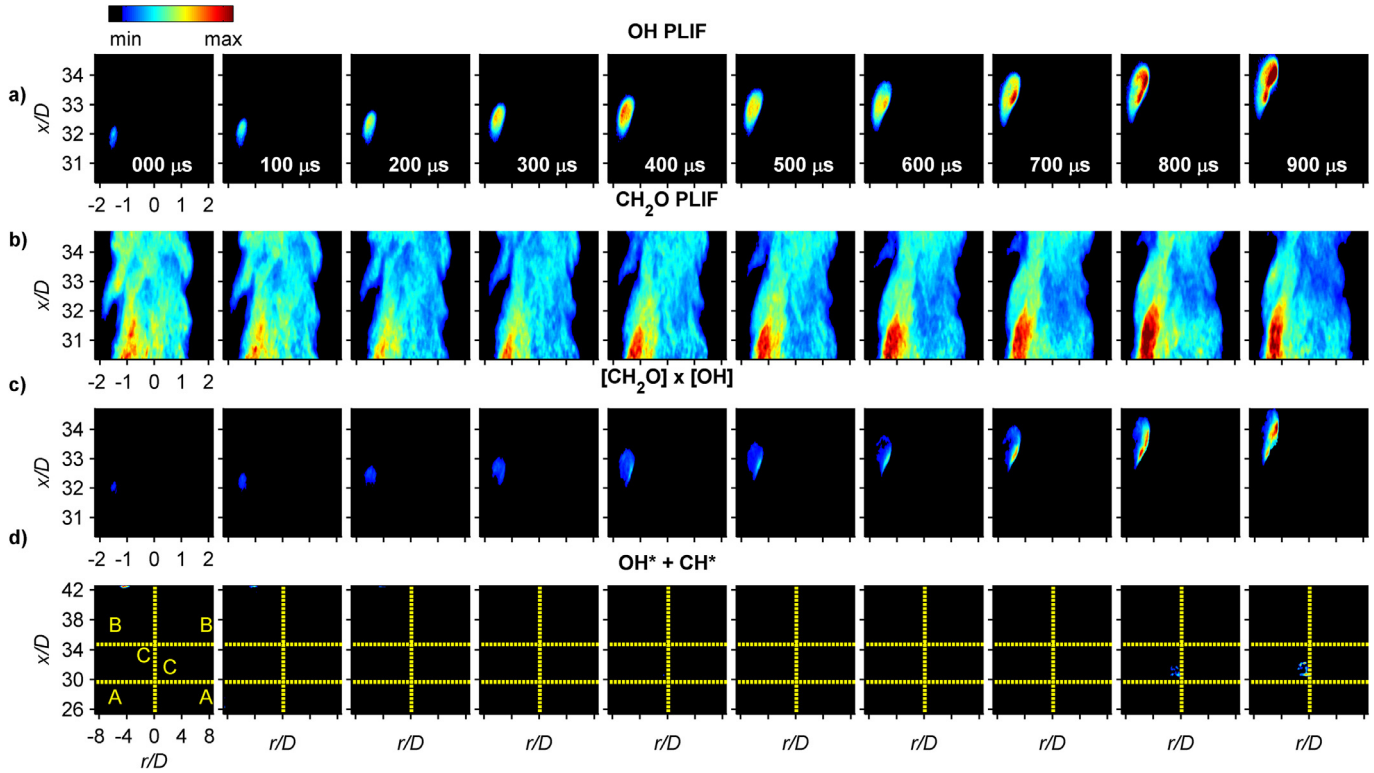

Fig. 4. Consecutive 10 kHz imaging for a $T_c = 1225$ K coflow igniting a pure DME fuel jet: OH PLIF (a) CH_2O PLIF (b) CH_2O x OH product (c) Perpendicular CH^* chemiluminescence (d).

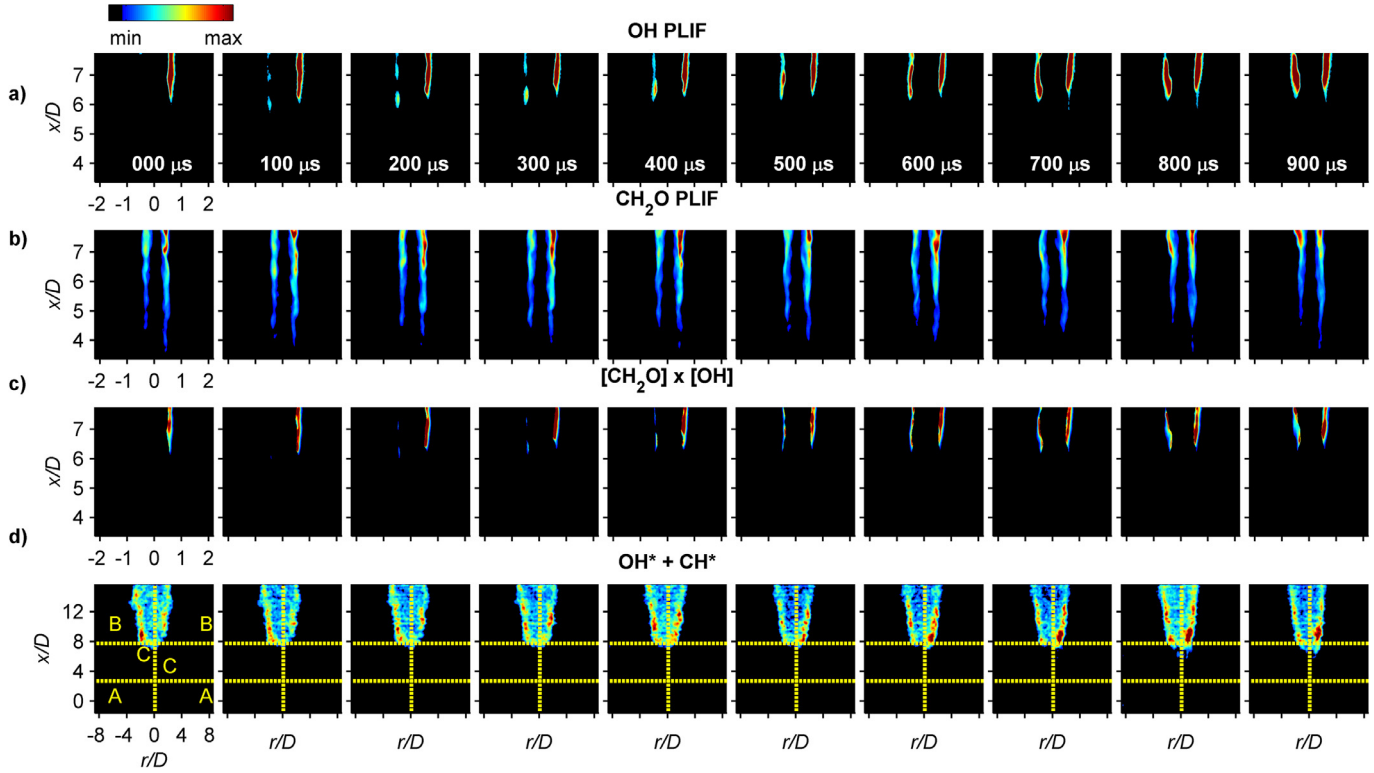

Fig. 5. Consecutive 10 kHz imaging for a $T_c = 1400$ K coflow igniting a pure DME fuel jet: OH PLIF (a) CH_2O PLIF (b) CH_2O x OH product (c) Perpendicular CH^* chemiluminescence (d).

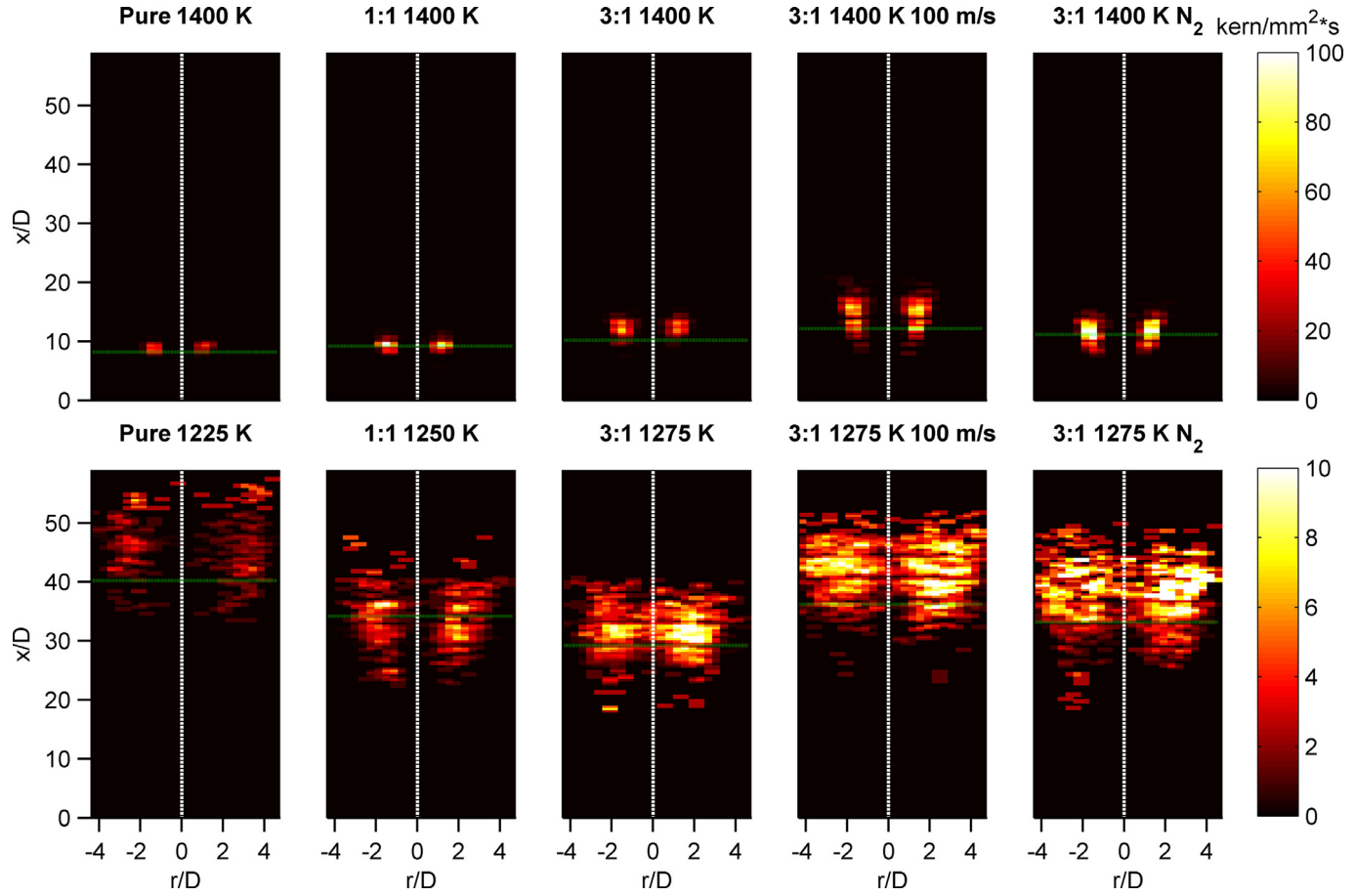

Fig. 6. OH-Kernel formation map for all flames studied: premixing ratios, velocity and dilution with N_2. Colour bars are given for an entire row, and they indicate spatial formation rates (kern/mm^2*s).

$T_c = 1400$ K for $U_J = 50$ m/s drastically increases the downstream location and axial range, for OH-kernel formation, albeit with a lower peak formation frequency. For a common coflow temperature of $T_c = 1400$ K, OH-kernels from a pure fuel jet form further upstream and have a reduced axial and radial formation range. Coflow temperatures lower than $T_c = 1400$ K produce, for the pure DME jet, OH-Kernels well outside of the centreline. However, with increasing premixing, such as the case with air:DME = 1:1, kernels move closer inwards. For the air:DME = 3:1 case with $T_c = 1275$ K, OH-kernels form along the centreline with increased probability of formation moving radially outwards.

Increasing the jet velocity to $U_J = 100$ m/s with air:DME = 3:1 moves the formation of OH-kernels further downstream for both the $T_c = 1400$ K and $T_c = 1275$ K coflow. Additionally, the axial range and formation rate of OH-kernels increase for increased jet velocity for both the high and low coflow temperatures. Finally, by analysing the spatial map of OH-kernels for high and low coflow temperatures, it is evident that at high T_c, kernels form further upstream in regions with potentially steeper mixture fraction gradients. Even though the low-temperature kernels are more spread axially and radially, they could be potentially across similar mixture fraction iso-contours as they are further downstream.

4.4. OH-kernel formation rates

The axial formation rates of OH-kernels are binned into increments of three jet diameters based on new OH-kernel centroids and are presented in Fig. 7. Formation rates are presented based on: air premixing and jet velocity, dilution or premixing and increased jet velocity ($U_J = 100$ m/s). The radial dimension has been 'collapsed' from the 2-D formation map presented previously in Fig. 6. The findings are summarized in bullet points below in regards to how varying partial premixing, coflow temperature and jet velocity effects OH-kernel formation: rates, location, and axial range.

- A reduction in coflow temperature is found to produce OH-kernels further downstream for all partial premixing cases. Additionally, the axial range is larger but more intermittent such that the temporal integration of formation rates is similar between high and low coflow temperatures for a given premixing case.
- Increased partial premixing for a common coflow temperature induces higher OH-kernel formation rates. The explanation for the increased formation rate is identified in Fig. 6, where kernels are forming with increased radial and axial range in the fuel jet, identifying that ignitable mixtures are more prevalent.
- A reduction in partial premixing is found to increase the axial range of kernel formation, noting that coflow temperatures between premixing cases were chosen based on similarity between lift-off heights. The axial broadening in formation rates is an attribute of the slower formation rate of reduced premixed jets; where a slower formation rate, in fact, creates a spatially broader formation range. A previous publication [60] has identified the downstream advection velocity of a pure DME fuel jet flame base is a lot slower than premixing of air:DME = 3:1; excluding kernel merging events. This decreased advection velocity explains how the formation rate can be slower while the lift-off height is similar.

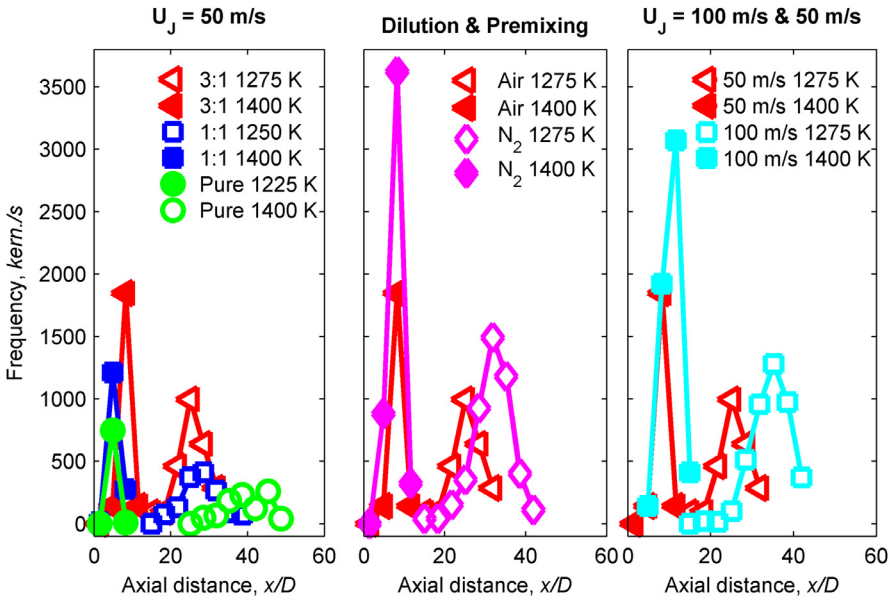

Fig. 7. New OH-Kernel formation rates for various coflow temperatures and diluents: Constant jet velocity ($U_J = 50$ m/s), varied dilution with constant 3:1 mixing (Dilution & Premixing) and varied jet velocity with constant air:DME = 3:1 premixing ($U_J = 100$ and 50 m/s).

- Results for OH-kernels at $U_J = 100$ m/s, air:DME = 3:1, indicate formation rates and the axial location for new OH-kernels increase for both high and low coflow temperatures. The increased rates may be due to the improved mixing rates induced by the higher shear between the fuel jet and coflow; further measurements are needed to ascertain this speculation.
- Jet dilution with nitrogen for the N_2:DME = 3:1 case seen in Fig. 7 leads to an increase in OH-kernel formation rates for both the $T_c = 1400$ K and $T_c = 1275$ K coflow. However, the peak formation rate shifts downstream, with this being more pronounced for the $T_c = 1275$ K coflow. The downstream shift in the formation rate is expected as the addition of an inert diluent reduces the reactivity of the mixture and hence increases the delay time for autoignition.
- Formation rates have previously been presented from chemiluminescence measurements [60] and these were found to be is five times lower than those obtained from the OH PLIF measurements in Fig. 7. The reduced formation rate emphasizes the finding in Fig. 4 where OH-kernels form well before chemiluminescence and in some instances OH-kernels are detected from PLIF measurements but not from chemiluminescence of CH*. Laminar calculations using a 1-D isobaric reactor and the NUIG Mech_56.54 mechanism [50] confirm that the initial formation of OH can form up to 1 ms earlier than CH*.
- Biasing of kernel formation rates from planar OH measurements may occur as a kernel that forms out of plane may then grow into the plane. The inter-plane growth would be registered as a new event increasing the formation rate: indicating that volumetric OH-LIF measurements are required to diagnose between out plane formation and inter-plane growth.

4.5. OH-kernel growth

Mean OH-kernel growth rates are presented in Fig. 8a based on one second of consecutive images collected at 10 kHz. The kernel size is defined by the OH-kernel projected onto the laser sheet, where the number of OH-kernel pixels is converted to mm^2 using the cameras pixel resolution. The OH-kernels grow larger than what is presented here of ~25 mm^2 for lower coflow temperatures (less than $T_c = 1400$ K). However, owing to the small OH-PLIF camera field of view, these kernels are excluded for further analysis and the reader is directed to another publication [60]. In this publication, chemiluminescence from low coflow temperature kernels grow up to 180 mm^2 for pure DME, 150 mm^2 for 1:1 and 130 mm^2 for 3:1 before merging with the flame base.

Growth rates are affected by in- and out-of-plane motion. However, mean values are presented here and these are found to be not affected by out-of-plane motion as confirmed by Meares et al. [71] for a non-premixed piloted burner.

In Fig. 8a there exists a linear relationship between size and evolution duration since the initiation of an OH-kernel. However, for all premixed and diluted cases studied here, the lower coflow temperatures yield OH-kernels that are growing faster. The duality in growth behaviour between coflow temperatures can be explained by analyzing Fig. 8b where the aspect ratio of a kernel (axial length/ width) for a given evolution time is presented. Again there is a separation between the aspect ratio from lower and higher coflow temperatures for a given premixing ratio, dilution and fuel velocity. Lower coflow temperatures (~$T_c = 1250$ K) all exhibit near unity aspect ratios identifying as is observed visually in Fig. 4 the kernels are circular in shape. However, higher coflow temperatures ($T_c = 1400$ K) have increased aspect ratios, indicating that they are no longer circular but elongated in the axial direction.

It is of interest that the aspect ratio of the OH-kernel with time or correspondingly with respect to size is not significantly changing; indicating they are growing preferentially along contours of similar mixture fractions. That is, the higher coflow temperature kernels form in an elongated manner and grow around its centroid, elongating slightly. Since the lower coflow temperature leads to the formation of OH-kernels further downstream, the spherical nature and growth could indeed be along similar contours of mixture fractions as the spatial mixture fraction gradients are not as steep. Furthermore, increases in coflow temperature, i.e., $T_c = 1400$ K, leads to the ignition of kernels with leaner mixture fractions and within regions of higher strain rates. This implies that at such high-temperature conditions, ignition and kernel growth could be occurring across a wider mixture fraction range.

Finally, the aspect ratios further indicate that for a constant premixed ratio at air:DME = 3:1 with varied injection velocities

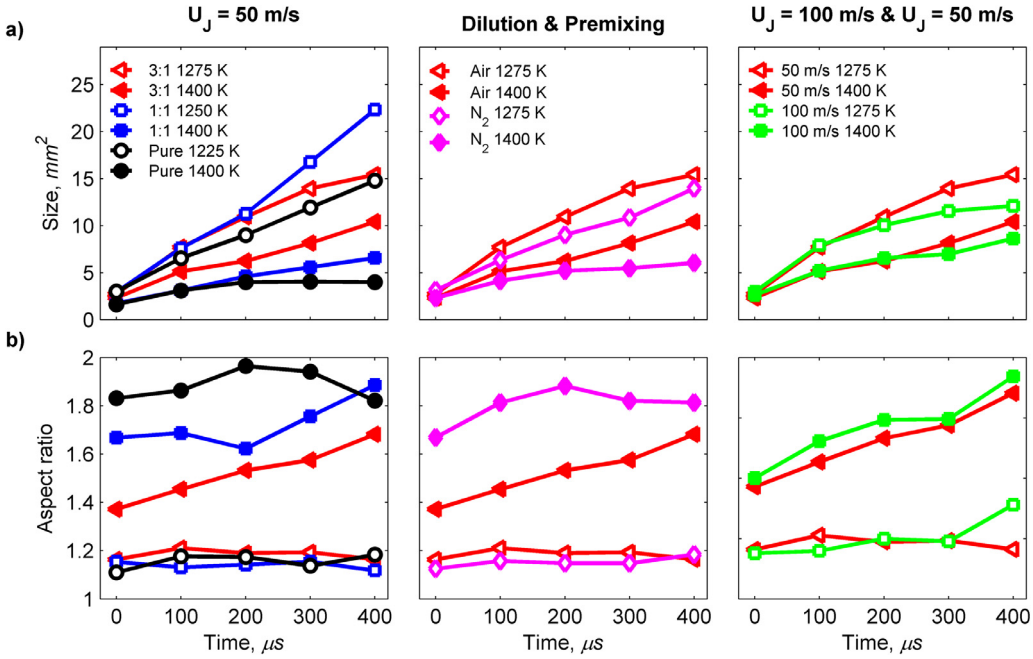

Fig. 8. OH-kernel growth with respect to time, based on size and aspect ratio: Row a) indicates size (mm^2). Row b) displays aspect ratios (kernel axial length divided by width). Columns separate constant jet velocity ($U_J = 50$ m/s), varied dilution with constant 3:1 mixing (Dilution & Premixing) and varying jet velocities for constant air:DME = 3:1 premixing ($U_J = 100$ and 50 m/s).

($U_J = 50$ m/s to $U_J = 100$ m/s) kernels are forming and growing with a similar shape. The similar aspect ratio leads implies that while the mixture fraction field is constant between fuel jet velocities, similar turbulence levels or scalar dissipation rates are required for the initiation of kernels. It is worth noting for increased velocity, $U_J = 100$ m/s, kernels are forming slightly further downstream as seen in Fig. 8.

4.6. Kernel signal intensities

Before analyzing the average heat release from autoignition events, a definition of the integrated heat release is required. The overlap of CH_2O onto the OH-kernel is employed here as a surrogate for heat release, where this correlation is confirmed in Fig. 2. Therefore, the heat release reported hereon is based on the product between an OH-kernel defined in Fig. 9 (OH Kernel) and the corresponding CH_2O signal that is projected onto it, Fig. 9 (CH_2O Kernel). Furthermore, the integrated kernel heat release is determined by the pixel sum from the product CH_2O x OH, Fig. 9 (CH_2O x OH), across the entire OH-kernel and their corresponding signal intensities.

An example of an ignition event for a high and low coflow temperature is seen in Fig. 9. It highlights for a low coflow temperature (a) that the peak OH signal is predominately in the centre of a kernel whilst the peak CH_2O signal is toward the OH-kernel edge. The product of the two signals, i.e., the heat release, moves relative to the OH and CH_2O signals and peak heat release occurs towards the upper region of the OH-kernel. A pixel threshold was selected for the CH_2O signal such that it just exceeds the background; therefore zero CH_2O counts are observed, and correspondingly zero heat release occurs. In Fig. 9b the higher coflow temperature, $T_c = 1400$ K, the kernel is elongated axially where the distribution of OH signal from the $T_c = 1225$ K and $T_c = 1400$ K cases are significantly different for these kernel samples. The low-temperature has a somewhat uniform OH gradient across both axes of the kernel, while the high-temperature has a radial OH gradient.

The signal distribution presented in Fig. 9 was for a single OH and HR-kernel, where distribution and intensities vary for different samples (seen in the scatter plots below), leading to fluctuating heat release levels. Furthermore, the signal intensities and spatial overlap vary for differing fuel mixtures and coflow temperatures. A summary of the peak signals and the average overlap of CH_2O onto OH are given in Table 3 for each fuel mixture based on the entire set of kernel events. The percentage of overlap relates to how much of the OH-kernel is overlapped by CH_2O above the threshold. A decrease in coflow temperature was found to increase the overlap, seen for the air:DME = 3:1 case between $T_c = 1275$ K and $T_c = 1400$ K given by 95% and 75% respectively.

Peak OH and CH_2O signals were found to be indicative of signals within ignition kernels (measured in the region of overlap) for various fuel mixtures. A decrease in coflow temperature somewhat surprisingly increases the signal strength for both OH and CH_2O within the kernel region for $U_J = 50$ m/s. The contrary is observed for the air:DME = 3:1 case with $U_J = 100$ m/s where the peak OH signal occurs for higher coflow temperatures.

4.7. Scatter plots: heat release, OH and CH_2O

While Table 3 presented the peak signals within kernels and the mean spatial overlap of OH onto CH_2O, it does not show the correlation between these species, nor does it provide any information about the heat release that occurs during various stages of kernel evolution. Having defined the spatial overlap in Fig. 9 of OH and CH_2O and how it affects the distribution of heat release within kernels; scatter plots for OH, CH_2O and HR signals are now presented in Fig. 10 for the case of air:DME = 3:1, and for two temperatures $T_c = 1275$ K and $T_c = 1400$ K. Two stages in the kernel evolution are given; for kernel initiation (triangles) and for 300 μs after initiation (circles).

It can be seen that the correlation of S_{OH} vs. S_{CH2O} is not monotonic for these kernels; that is, a kernel with large S_{OH} does not correspond distinctly to a low S_{CH2O}. However, as a kernels grow over 300 μs, the average CH_2O signal can be seen to decrease

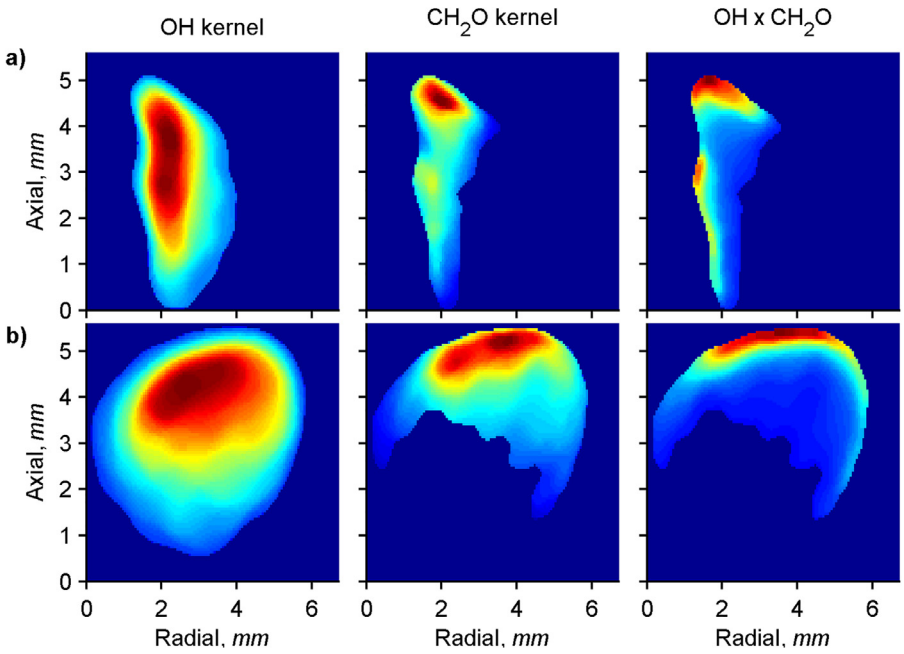

Fig. 9. A single autoignition event for a high and low coflow temperature: $Tc = 1225$ K (a) and $Tc = 1400$ K (b), for a Pure DME jet. Displayed is an OH-kernel, the CH_2O overlap (projection) and product CH_2O x OH (HR-kernel).

Table 3
Spatial overlap of CH_2O onto an OH-kernel and their peak signals for all OH-kernels observed for varying: coflow temperatures, premixing and jet velocities.

Mixing ratio (U_J)	Pure DME (50 m/s)		air:DME = 1:1 (50 m/s)		air:DME = 3:1 (50 m/s)		N_2:DME = 3:1 (50 m/s)		air:DME = 3:1 (100 m/s)	
T_c (K)	1400	1225	1400	1250	1400	1275	1400	1275	1400	1275
Peak CH_2O (Counts)	433	907	433	563	481	574	509	647	518	617
Overlap (%)	50	99	30	95	75	95	40	60	60	92
Peak OH (Counts)	1028	2096	1028	1988	772	1069	1748	2116	2187	961

whilst the OH signal increases. The change in these signals with kernel evolution is expected as the low-temperature build-up of CH_2O is consumed, leading to higher temperature reactions involving OH. For the heat release (S_{CH2O} x S_{OH}) vs. S_{OH}, a somewhat monotonic correlation is observed, where increasing OH levels lead to increased heat release. The slopes for the HR vs. S_{OH} plots shown in Fig. 10 (middle column) are labelled C_0 and C_1, respectively for the times during kernel initiation and 300 µs after. It is evident that the gradient of the scatter has decreased as ignition progresses ($C_1 < C_0$). The decreasing gradient indicates that as a kernel grows, the HR doesn't correlate to increasing OH levels and therefore CH_2O and its overlap has a somewhat larger influence on the heat release.

For HR vs S_{CH2O} the scatter is further decreased, compared to S_{OH}, and the near linear relationship is improved. The slopes for the for the HR vs. S_{CH2O} plots are shown in Fig. 10 (right column) and are labelled D_0 and D_1 for the two times during kernel initiation and 300 µs after. Contrarily to the slopes of HR vs. S_{OH}, the trends here are reversed so that the gradient for 300 µs after ignition is now higher with $D_1 > D_0$ (instead of $C_1 < C_0$ as observed earlier for HR vs. S_{OH}). Therefore, as described in Table 3 the overlap and CH_2O intensity has a large influence into the heat released from a kernel. Reduced scatter for S_{CH2O}, whilst indicating a stronger correlation to heat release, could be an artefact of the kernel being defined by the OH kernel contour. That is, the low-temperature radical, CH_2O would occur upstream of OH being present leading to a reduction in the correlation between HR vs. S_{CH2O}.

The lower coflow temperature, $T_c = 1275$ K, compared to $T_c = 1400$ K, has a larger OH signal for all time intervals, whilst CH_2O is similar for both temperatures. The increase in signal levels, in addition to the increased signal overlap as described in Table 3, leads to increased heat release levels for the lower coflow temperature. However, the correlation (monotonic relationship) between HR-OH and between HR-CH_2O (reflected in the slopes C_1, C_0 and D_1, D_0) in Fig. 10 is similar for the high and low coflow temperatures, including the varying correlation with kernel growth. It is noted that the trends observed here for the air:DME = 3:1 case are reflected also for other premixing ratios (not shown) studied in this paper.

4.8. Integrated kernel heat release with size

The average integrated heat release for varying HR-kernel sizes is displayed in Fig. 11 for all cases listed in Table 1, where a linear relationship between kernel size and time was shown in Fig. 8.

Kernel heat release was normalized with size to indicate that heat release is growing proportionally to kernel size, shown by the horizontal lines in Fig. 11. The linear correlation between heat release and size indicates that whilst heat release forms on part of a kernel edge, seen in Fig. 4c, it grows proportionally to the kernel area. Note that a quadratic relationship would exist if the heat release were to be uniform across a growing kernel.

An interesting finding is the degree of difference between the high and low coflow temperatures; increased coflow temperature, in fact, decreases the heat release. The difference in heat release

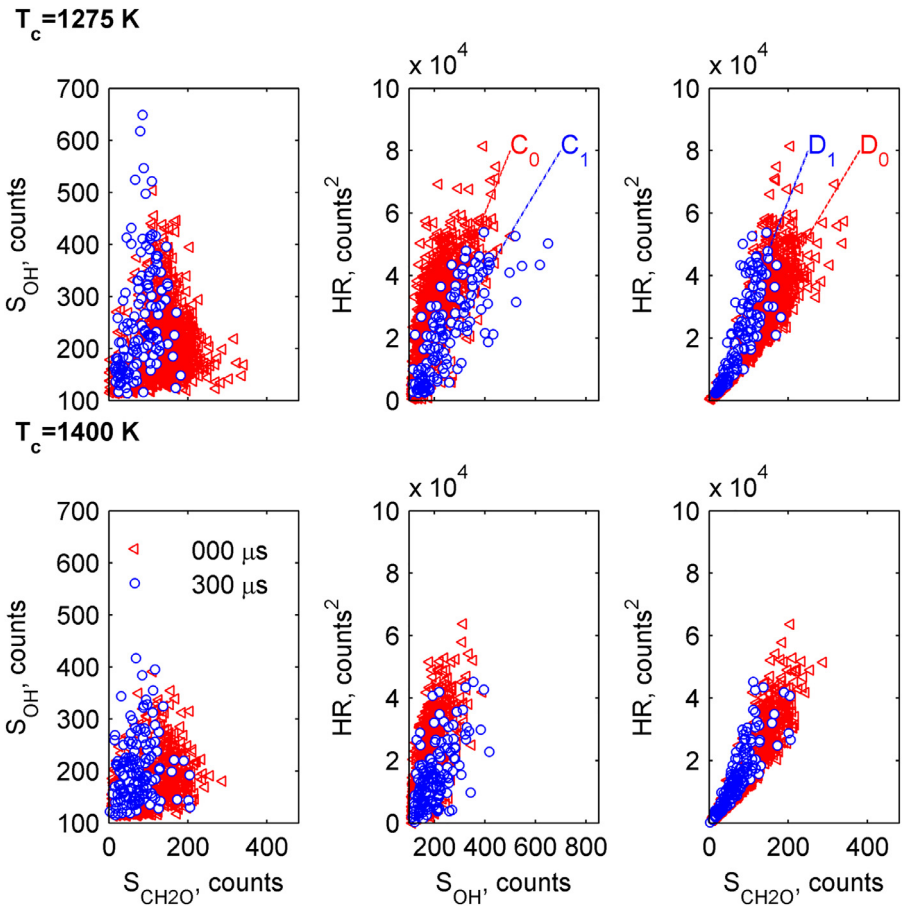

Fig. 10. Scatter plots for OH, CH_2O and HR signal counts for the case of air:DME = 3:1, and for two temperatures $T_c = 1275$ K (top row) and $T_c = 1400$ K (bottom row). Left: correlation of signals S_{OH} vs. S_{CH2O}; middle: correlation of HR vs. $S_{OH;}$ right: correlation of HR vs. S_{CH2O} Each plot shows two stages in the kernel evolution; for kernel initiation (triangles) and for 300 µs after initiation (circles). The dashed lines shown are the slopes C_0, D_0 are for kernel initiation and C_1, D_1 for 300 µs after initiation.

is predominately attributed to lower coflow temperatures having a larger spatial overlap of CH_2O onto an OH kernel as observed in Table 3. The increased spatial overlap is in addition to higher OH and CH_2O signal intensities for lower coflow temperatures.

It is seen in Fig. 11 that heat release increases with reduced partial premixing for coflow temperatures less than $T_c = 1400$ K. Pure DME for $T_c = 1225$ K produces more integrated heat release than air:DME = 1:1 at $T_c = 1250$ K followed by air:DME = 3:1 at $T_c = 1275$ K. It is interesting that whilst the air:DME = 3:1 cases are bimodal between high and low coflow temperatures, the degree of bimodality is reduced.

The effect of N_2 dilution has increased the separation of heat release between the high and low coflow temperature seen in Fig. 11 (Dilution). The high coflow temperature ($T_c = 1400$ K) has increased occurrences for low heat releasing kernels which are a direct correlation of the reduction in CH_2O and OH. The distribution between OH and CH_2O for $T_c = 1275$ K N_2:DME = 3:1 is similar to that of air:DME = 3:1, leading to the similar levels of heat release. Increased velocity, $U_J = 100$ m/s, has done very little to change the heat release levels for a high and low coflow temperature despite $T_c = 1400$ K kernels producing more OH signal.

The observed linearity of average integrated heat release with increased kernel size indicates the signal distribution and intensities do not vary significantly during growth. That is, the average CH_2O signal decreases slightly across an OH-kernel while the average OH signal increases slightly for an increase in size. Indicating, size or amount of overlap has a larger influence on the integrated heat release. There is a relatively strong correlation between the kernel aspect ratios observed in Fig. 8 and the heat release profiles from Fig. 11. For example, in the pure DME jet case the high-temperature coflow, $T_c = 1400$ K, has a large kernel aspect ratio (~1.9) and corresponding low heat release. While the low-temperature coflow, $T_c = 1225$ K, has a small aspect ratio (~1.2) and a relatively high heat release. If the aspect ratio is indicative of the spatial mixture fraction gradient of a kernel as mentioned in Section 4.5, the heat release is also proportional to the relative ignitable mixture fraction. Therefore, this potentially means the higher coflow temperature kernels are igniting in leaner regions than low coflow temperatures (still igniting in lean mixtures) which would lead to lower heat release.

4.9. Integrated heat release fluctuations

There are numerous occasions for all fuel cases listed in Table 1 where there is up to two orders of magnitude difference for the heat intensity for a given kernel size. The PDF of heat intensities are presented in Fig. 12 for two kernel sizes; 1 mm^2 is deemed to be kernel formation and increasing size indicates different stages of kernel propagation.

The variation in heat release for differently sized kernels is attributed to fluctuating levels of OH and CH_2O overlap, their respective signal intensities and distribution throughout an OH-kernel. Therefore, it is identified that there are instances where a kernel is burning intensely and is providing significant heat to the flame base. However, there are other occasions where they are seemingly less fundamental to the heat released into the flame base and

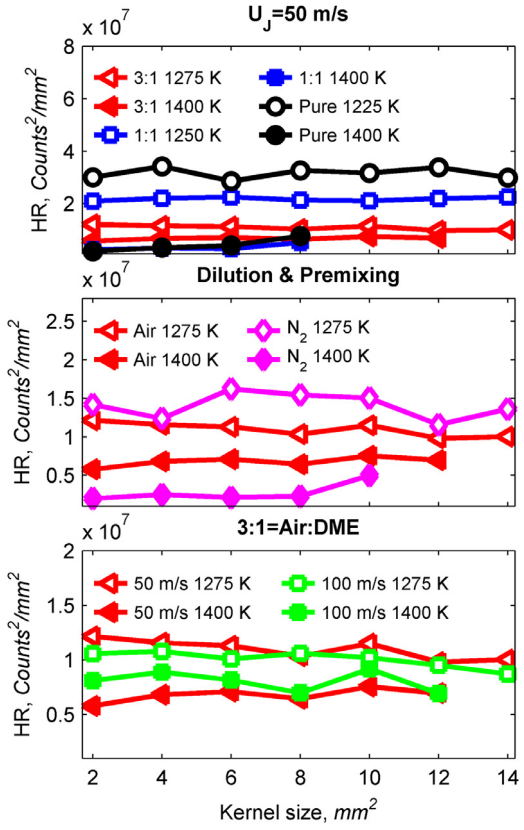

Fig. 11. Average integrated heat release normalized heat release ([CH_2O] x [OH]) for kernel sizes at 1 mm^2 bins. Rows describe: constant jet velocity ($U_J = 50$ m/s), varied dilution with constant 3:1 mixing (Dilution & Premixing) and varying jet velocities for constant Air:DME = 3:1 premixing ($U_J = 100$ and 50 m/s).

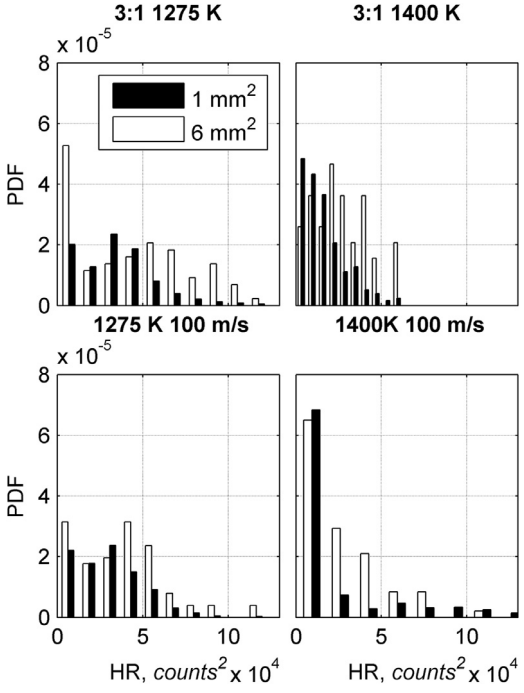

Fig. 12. Size normalized heat release (CH_2O x OH) PDF for varying diluents and coflow temperatures. A 1 mm^2 kernel represents kernel initiation.

hence to the stabilization process. Normalizing with kernel size has produced overlapping PDFs for differing kernel sizes, verifying that kernel size is attributed to increased integrated heat release opposed to varying overlap or signal strength as a kernel propagates. Furthermore, there are occasions where the 1 mm^2 kernel can be burning more intensely than larger kernels.

For high coflow temperatures ($T_c = 1400$ K), the pdf is strongly 'skewed' to the right i.e., reduced heat release, verifying why the integrated average heat release in Fig. 11 is smaller for increased coflow temperature. The increased probability for high coflow temperatures producing less heat release is more pronounced for pure DME (not displayed). Stabilization due to autoignition is theorized to produce kernels that are significant to stabilization and have high reactivity/heat release, where this is observed for low coflow temperatures. Higher coflow temperatures have minimal heat releasing kernels and therefore it is theorized to be stabilized by flame propagation in addition to autoignition events.

The PDF makes it possible to identify how the increased velocity ($U_J = 100$ m/s) for air:DME = 3:1, $T_c = 1400$ K can have instances where a kernel has larger peak OH (Table 3) and heat release intensities (Fig. 12) than the $T_c = 1275$ K $U_J = 50$ m/s case, while the overall average heat release is less given by Fig. 11. The smaller average heat release for increased velocity is due to an even greater left skew for $T_c = 1400$ K, with more occurrences of kernels having minimal heat release. The range in heat release for increased velocity may be due to increased turbulence producing both higher scalar dissipation and similar dissipative levels to the lower $U_J = 50$ m/s case; however, this requires further investigation.

5. Conclusion

This paper presents an experimental study of the autoignition characteristics of DME using a jet in a hot vitiated coflow burner. A range of jet dilution and partial premixing ratios are studied for high ($T_c = 1400$ K) and low coflow ($T_c = 1225$–1275 K) temperatures corresponding to a low stable flame and a lifted flame respectively. High repetition rate (10 kHz) joint imaging of PLIF OH and CH_2O is performed along with imaging of chemiluminescence to monitor the temporal and spatial evolution of ignition kernels and their movement in and out of the imaging plane. The following conclusions are drawn:

- The lift-off heights and hence regions of OH formation are further downstream when the coflow temperature is low. Formaldehyde forms upstream of OH, and significant levels occur upstream of the flame base for relatively low coflow temperatures. The pooling of CH_2O upstream of OH agrees with other studies with simpler fuels such as CH_4 [6] for the same hot vitiated coflow burner.
- By using high-speed imaging, kernel formation events could be identified, where kernels occur upstream of the main stabilization zone at both low and high coflow temperatures. The kernels occur further downstream with increased axial range at lower coflow temperatures.
- For a constant coflow temperature, the effect of premixing air with fuel in the jet is to increase the kernel formation rate and increase the mean lift-off height. The higher formation rate with increased premixing therefore indicates that kernel formation rate is not solely a good indication of flame stabilization. The kernel formation rate alone is not sufficient to explain the differences in flame stabilization with increased premixing. The drift velocity or advection rate of the flame base is needed to explain this behaviour whereby an increase in advection is noted with increasing premixing of air in the DME. This finding is consistent with previous results using chemiluminescence

imaging [60] which show that the downstream flame base advection of a pure DME jet is slower.

- The product of CH_2O x OH LIF signals was used as a heat release marker for DME where its use was validated from transient opposed flow simulations. Therefore, the spatial overlap between the OH and CH_2O LIF images was used as a surrogate for heat release in ignition kernels.
- Within a given autoignition kernel a large range of CH_2O signals was found, correlating with a multitude of OH levels. However, for increasing CH_2O levels, there was a broad correlation of increasing heat release; this correlation was found to be much stronger than that of OH and heat release.
- The amount of integrated heat release has a linear correlation with kernel size, which indicates the relative overlap and intensities of OH and CH_2O do not vary significantly during kernel evolution. That is heat release is predominantly produced on a single kernel edge and grows at a proportional rate to the kernel area.
- Lower coflow temperatures produced kernels with greater heat release relative to the high coflow temperatures. The OH and CH_2O signal levels vary slightly between high and low coflow temperatures, however, spatial overlap of CH_2O onto OH varies the greatest; with lower coflow temperatures having a larger overlap.
- The relatively small heat release for a high coflow temperature is seemingly correlated with the large aspect ratio of a kernel (axial elongation). Assuming that the aspect ratio is indicative to mixture fraction gradients it identifies that kernels from hotter coflow temperatures ignite in leaner regions, in regions of steeper mixture fraction gradients.

The results presented in this paper have explored kernel evolution and heat release exclusively for DME. The use of DME as a fuel in this study allows the sustained high-speed PLIF of CH_2O at relatively low laser energies (3.3 mJ/pulse) with high SNR; other fuels such as CH_4 require significantly more energy, an order of magnitude greater. DME despite being a more complex fuel with mild NTC characteristics behaves at least with respect to lift-off heights and its dependence on coflow temperatures, similarly to simpler fuels such as H_2 and CH_4. The varying levels of kernel heat release due to coflow temperatures are hypothesized to be primarily influenced by ignition kernels propagating in differing mixtures. The higher coflow temperatures are seemingly igniting at leaner mixtures with steeper mixture fraction gradients. Further measurements of composition and mixture fraction space would provide deeper insight into the structure around kernel evolution events identified in this paper.

Acknowledgments

This work was supported by the Australian Research Council Equipment grant LE110100225.

References

[1] C. Arcoumanis, C. Bae, R. Crookes, E. Kinoshita, The potential of di-methyl ether (DME) as an alternative fuel for compression-ignition engines: a review, Fuel 87 (2008) 1014–1030.
[2] M.C. Lee, S.B. Seo, J.H. Chung, Y.J. Joo, D.H. Ahn, Industrial gas turbine combustion performance test of DME to use as an alternative fuel for power generation, Fuel 88 (2009) 657–662.
[3] C.S. Yoo, E.S. Richardson, R. Sankaran, J.H. Chen, A DNS study on the stabilization mechanism of a turbulent lifted ethylene jet flame in highly-heated coflow, Proc. Combust. Inst. 33 (2011) 1619–1627.
[4] R. Cabra, J.Y. Chen, R.W. Dibble, A.N. Karpetis, R.S. Barlow, Lifted methane–air jet flames in a vitiated coflow, Combust. Flame 143 (2005) 491–506.
[5] R. Cabra, T. Myhrvold, J.Y. Chen, R.W. Dibble, A.N. Karpetis, R.S. Barlow, Simultaneous laser Raman–Rayleigh-lif measurements and numerical modeling results of a lifted turbulent H_2/N_2 jet flame in a vitiated coflow, Proc. Combust. Inst 29 (2002) 1881–1888.
[6] R.L. Gordon, A.R. Masri, E. Mastorakos, Simultaneous Rayleigh temperature, OH- and CH_2O-LIF imaging of methane jets in a vitiated coflow, Combust. Flame 155 (2008) 181–195.
[7] R.L. Gordon, S.H. Stårner, A.R. Masri, R.W. Bilger, Further characterisation of lifted hydrogen and methane flames issuing into a vitiated coflow, 5th Asia–Pacific Conference on Combustion, University of Adelaide (2005), pp. 333–336.
[8] E. Oldenhof, M.J. Tummers, E.H. van Veen, D.J.E.M. Roekaerts, Conditional flow field statistics of jet-in-hot-coflow flames, Combust. Flame 160 (2013) 1428–1440.
[9] E. Oldenhof, M.J. Tummers, E.H. van Veen, D.J.E.M. Roekaerts, Ignition kernel formation and lift-off behaviour of jet-in-hot-coflow flames, Combust. Flame 157 (2010) 1167–1178.
[10] E. Oldenhof, M.J. Tummers, E.H. van Veen, D.J.E.M. Roekaerts, Role of entrainment in the stabilisation of jet-in-hot-coflow flames, Combust. Flame 158 (2011) 1553–1563.
[11] E. Oldenhof, M.J. Tummers, E.H. van Veen, D.J.E.M. Roekaerts, Transient response of the Delft jet-in-hot coflow flames, Combust. Flame 159 (2012) 697–706.
[12] C.M. Arndt, J.D. Gounder, W. Meier, M. Aigner, Auto-ignition and flame stabilization of pulsed methane jets in a hot vitiated coflow studied with high-speed laser and imaging techniques, Appl. Phys. B 108 (2012) 407–417.
[13] C.M. Arndt, R. Schießl, J.D. Gounder, W. Meier, M. Aigner, Flame stabilization and auto-ignition of pulsed methane jets in a hot coflow: influence of temperature, Proc. Combust. Inst. 34 (2013) 1483–1490.
[14] C.N. Markides, E. Mastorakos, An experimental study of hydrogen autoignition in a turbulent co-flow of heated air, Proc. Combust. Inst. 30 (2005) 883–891.
[15] P.R. Medwell, B.B. Dally, Experimental observation of lifted flames in a heated and diluted coflow, Energ Fuels 26 (2012) 5519–5527.
[16] P.R. Medwell, P.A.M. Kalt, B.B. Dally, Imaging of diluted turbulent ethylene flames stabilized on a Jet in Hot Coflow (JHC) burner, Combust. Flame 152 (2008) 100–113.
[17] P.R. Medwell, P.A.M. Kalt, B.B. Dally, Simultaneous imaging of OH, formaldehyde, and temperature of turbulent nonpremixed jet flames in a heated and diluted coflow, Combust. Flame 148 (2007) 48–61.
[18] B. Johannessen, A. North, R. Dibble, T. Løvås, Experimental studies of autoignition events in unsteady hydrogen–air flames, Combust. Flame 162 (2015) 3210–3219.
[19] Z. Wu, A.R. Masri, R.W. Bilger, An experimental investigation of the turbulence structure of a lifted h2/n2 jet flame in a vitiated co-flow, Flow. Turb. Combust. 76 (2006) 61–81.
[20] C. Duwig, M.J. Dunn, Large Eddy Simulation of a premixed jet flame stabilized by a vitiated co-flow: evaluation of auto-ignition tabulated chemistry, Combust. Flame 160 (2013) 2879–2895.
[21] J. Ye, P.R. Medwell, M.J. Evans, B.B. Dally, Characteristics of turbulent n-heptane jet flames in a hot and diluted coflow, Combust. Flame 183 (2017) 330–342.
[22] C.M. Arndt, M.J. Papageorge, F. Fuest, J.A. Sutton, W. Meier, M. Aigner, The role of temperature, mixture fraction, and scalar dissipation rate on transient methane injection and auto-ignition in a jet in hot coflow burner, Combust. Flame 167 (2016) 60–71.
[23] M.J. Papageorge, C. Arndt, F. Fuest, W. Meier, J.A. Sutton, High-speed mixture fraction and temperature imaging of pulsed, turbulent fuel jets auto-igniting in high-temperature, vitiated co-flows, Exp. Fluids 55 (2014) 1763.
[24] E. Mastorakos, T.A. Baritaud, T.J. Poinsot, Numerical simulations of autoignition in turbulent mixing flows, Combust. Flame 109 (1997) 198–223.
[25] R. Hilbert, D. Thévenin, Autoignition of turbulent non-premixed flames investigated using direct numerical simulations, Combust. Flame 128 (2002) 22–37.
[26] T. Echekki, J.H. Chen, High-temperature combustion in autoigniting non-homogeneous hydrogen/air mixtures, Proc. Combust. Inst. 29 (2002) 2061–2068.
[27] S. Sreedhara, K.N. Lakshmisha, Autoignition in a non-premixed medium: DNS studies on the effects of three-dimensional turbulence, Proc. Combust. Inst. 29 (2002) 2051–2059.
[28] S. Cao, T. Echekki, Autoignition in nonhomogeneous mixtures: Conditional statistics and implications for modeling, Combust. Flame 151 (2007) 120–141.
[29] E. Mastorakos, Ignition of turbulent non-premixed flames, Prog. Energy Combust. Sci. 35 (2009) 57–97.
[30] C.S. Yoo, R. Sankaran, J.H. Chen, Three-dimensional direct numerical simulation of a turbulent lifted hydrogen jet flame in heated coflow: flame stabilization and structure, J. Fluid Mech. 640 (2009) 453–481.
[31] R.L. Gordon, A.R. Masri, S.B. Pope, G.M. Goldin, A numerical study of auto-ignition in turbulent lifted flames issuing into a vitiated co-flow, Combust. Theor. Model. 11 (2007) 351–376.
[32] R.L. Gordon, A.R. Masri, S.B. Pope, G.M. Goldin, Transport budgets in turbulent lifted flames of methane autoigniting in a vitiated co-flow, Combust. Flame 151 (2007) 495–511.
[33] K. Gkagkas, R.P. Lindstedt, Transported PDF modelling with detailed chemistry of pre- and auto-ignition in CH4/air mixtures, Proc. Combust. Inst. 31 (2007) 1559–1566.
[34] O. Schulz, T. Jaravel, T. Poinsot, B. Cuenot, N. Noiray, A criterion to distinguish autoignition and propagation applied to a lifted methane–air jet flame, Proc. Combust. Inst. 36 (2017) 1637–1644.
[35] S. Deng, P. Zhao, M.E. Mueller, C.K. Law, Autoignition-affected stabilization of laminar nonpremixed DME/air coflow flames, Combust. Flame 162 (2015) 3437–3445.
[36] A.R. Masri, R. Cao, S.B. Pope, G.M. Goldin, Pdf calculations of turbulent lifted

flames of H2/N2 fuel issuing into a vitiated co-flow, Combust. Theor. Model. 8 (2004) 1–22.
[37] S. Navarro-Martinez, A. Kronenburg, LES–CMC simulations of a lifted methane flame, Proc. Combust. Inst. 32 (2009) 1509–1516.
[38] P. Domingo, L. Vervisch, D. Veynante, Large-eddy simulation of a lifted methane jet flame in a vitiated coflow, Combust. Flame 152 (2008) 415–432.
[39] H. Haessler, H. Bockhorn, C. Pfeifer, D. Kuhn, Formaldehyde-LIF of dimethyl ether during auto-ignition at elevated pressures, Flow. Turb. Combust. 89 (2011) 249–259.
[40] G. Fast, D. Kuhn, A.G. Class, U. Maas, Auto-ignition during instationary jet evolution of dimethyl ether (DME) in a high-pressure atmosphere, Combust. Flame 156 (2009) 200–213.
[41] R.L. Gordon, A.R. Masri, E. Mastorakos, Heat release rate as represented by $[OH] \times [CH_2O]$ and its role in autoignition, Combust. Theor. Model. 13 (2009) 645–670.
[42] F. Eitel, J. Pareja, A. Johchi, B. Böhm, D. Geyer, A. Dreizler, Temporal evolution of auto-ignition of ethylene and methane jets propagating into a turbulent hot air co-flow vitiated with NOx, Combust. Flame 177 (2017) 193–206.
[43] A. Joedicke, N. Peters, M. Mansour, The stabilization mechanism and structure of turbulent hydrocarbon lifted flames, Proc. Combust. Inst. 30 (2005) 901–909.
[44] M. Röder, T. Dreier, C. Schulz, Simultaneous measurement of localized heat release with OH/CH_2O-LIF imaging and spatially integrated OH^* chemiluminescence in turbulent swirl flames, Appl. Phys. B 107 (2012) 611–617.
[45] P.H. Paul, H.N. Najm, Planar laser-induced fluorescence imaging of flame heat release rate, Symp. (Int.) Combust. 27 (1998) 43–50.
[46] B.C. Choi, S.H. Chung, Autoignited laminar lifted flames of methane, ethylene, ethane, and n-butane jets in coflow air with elevated temperature, Combust. Flame 157 (2010) 2348–2356.
[47] B.C. Choi, K.N. Kim, S.H. Chung, Autoignited laminar lifted flames of propane in coflow jets with tribrachial edge and mild combustion, Combust. Flame 156 (2009) 396–404.
[48] P.R. Medwell, D.L. Blunck, B.B. Dally, The role of precursors on the stabilisation of jet flames issuing into a hot environment, Combust. Flame 161 (2014) 465–474.
[49] H.J. Curran, W.J. Pitz, C.K. Westbrook, P. Dagaut, J.C. Boettner, M. Cathonnet, A wide range modeling study of dimethyl ether oxidation, Int. J. Chem. Kinet. 30 (1998) 229–241.
[50] U. Burke, K.P. Somers, P. O'Toole, C.M. Zinner, N. Marquet, G. Bourque, E.L. Petersen, W.K. Metcalfe, Z. Serinyel, H.J. Curran, An ignition delay and kinetic modeling study of methane, dimethyl ether, and their mixtures at high pressures, Combust. Flame 162 (2015) 315–330.
[51] W.K. Metcalfe, S.M. Burke, S.S. Ahmed, H.J. Curran, A hierarchical and comparative kinetic modeling study of C1 – C2 hydrocarbon and oxygenated fuels, Int. J. Chem. Kinet. 45 (2013) 638–675.
[52] Z. Zhao, M. Chaos, A. Kazakov, F.L. Dryer, Thermal decomposition reaction and a comprehensive kinetic model of dimethyl ether, Int. J. Chem. Kinet. 40 (2008) 1–18.
[53] L. Pan, E. Hu, F. Deng, Z. Zhang, Z. Huang, Effect of pressure and equivalence ratio on the ignition characteristics of dimethyl ether-hydrogen mixtures, Int. J. Hydrogen Energy 39 (2014) 19212–19223.
[54] L. Pan, E. Hu, Z. Tian, F. Yang, Z. Huang, Experimental and kinetic study on ignition delay times of dimethyl ether at high temperatures, Energy Fuels 29 (2015) 3495–3506.
[55] L. Pan, S. Kokjohn, Z. Huang, Development and validation of a reduced chemical kinetic model for dimethyl ether combustion, Fuel 160 (2015) 165–177.
[56] N.L. Le Tan, M. Djehiche, C.D. Jain, P. Dagaut, G. Dayma, Quantification of HO_2 and other products of dimethyl ether oxidation (H_2O_2, H_2O, and CH_2O) in a jet-stirred reactor at elevated temperatures by low-pressure sampling and continuous-wave cavity ring-down spectroscopy, Fuel 158 (2015) 248–252.
[57] T. Echekki, S.F. Ahmed, Turbulence effects on the autoignition of DME in a turbulent co-flowing jet, Combust. Flame 178 (2017) 70–81.
[58] A. Liñán, The asymptotic structure of counterflow diffusion flames for large activation energies, Acta Astronaut. 1 (1974) 1007–1039.
[59] X.L. Zheng, T.F. Lu, C.K. Law, C.K. Westbrook, H.J. Curran, Experimental and computational study of nonpremixed ignition of dimethyl ether in counterflow, Proc. Combust. Inst 30 (2005) 1101–1109.
[60] A.R.W. Macfarlane, M.J. Dunn, M. Juddoo, A.R. Masri, Stabilisation of turbulent auto-igniting dimethyl ether jet flames issuing into a hot vitiated coflow, Proc. Combust. Inst. 36 (2017) 1661–1668.
[61] D.G. Goodwin, H.K. Moffat, R.L. Speth, Cantera: An object- oriented software toolkit for chemical kinetics, thermodynamics, and transport processes. http://code.google.com/p/cantera, 2012.
[62] M. Tamura, P.A. Berg, J.E. Harrington, J. Luque, J.B. Jeffries, G.P. Smith, D.R. Crosley, Collisional Quenching of CH(A), OH(A), and NO(A) in Low Pressure Hydrocarbon Flames, Combust. Flame 114 (1998) 502–514.
[63] B.O. Ayoola, R. Balachandran, J.H. Frank, E. Mastorakos, C.F. Kaminski, Spatially resolved heat release rate measurements in turbulent premixed flames, Combust. Flame 144 (2006) 1–16.
[64] B. Coriton, M. Zendehdel, S. Ukai, A. Kronenburg, O.T. Stein, S.-K. Im, M. Gamba, J.H. Frank, Imaging measurements and LES-CMC modeling of a partially-premixed turbulent dimethyl ether/air jet flame, Proc. Combust. Inst. 35 (2015) 1251–1258.
[65] S. Popp, F. Hunger, S. Hartl, D. Messig, B. Coriton, J.H. Frank, F. Fuest, C. Hasse, LES flamelet-progress variable modeling and measurements of a turbulent partially-premixed dimethyl ether jet flame, Combust. Flame 162 (2015) 3016–3029.
[66] Y. Yamasaki, A. Tezaki, Non-linear pressure dependence of A-state fluorescence lifetime of formaldehyde, Appl. Phys. B 80 (2005) 791–795.
[67] K. Shibuya, E.K.C. Lee, Vibrational and electronic energy transfers from a single vibronic level of H_2CO (A, 1A,2), the 41 level, J. Chem. Phys. 69 (1978) 758.
[68] D.C. Kyritsis, V.S. Santoro, A. Gomez, The effect of temperature correction on the measured thickness of formaldehyde zones in diffusion flames for 355 nm excitation, Exp. Fluids 37 (2004) 769–772.
[69] DJ Clouthier, D.A. Ramsay, The spectroscopy of formaldehyde and thioformaldehyde, Annu. Rev. Phys. Chem. 34 (1983) 31–58.
[70] S.M. Al-Noman, S.K. Choi, S.H. Chung, Numerical study of laminar nonpremixed methane flames in coflow jets: autoignited lifted flames with tribrachial edges and MILD combustion at elevated temperatures, Combust. Flame 171 (2016) 119–132.
[71] S. Meares, V.N. Prasad, M. Juddoo, K.H. Luo, A.R. Masri, Simultaneous planar and volume cross-LIF imaging to identify out-of-plane motion, Proc. Combust. Inst. 35 (2015) 3813–3820.